2023 IEEE International Conference on Robotics and Automation (ICRA 2023)
May 29 - June 2, 2023. London, UK

Design and Control of a Micro Overactuated Aerial Robot with an Origami Delta Manipulator

Eugenio Cuniato[1], Christian Geckeler[2], Maximilian Brunner[1], Dario Strübin[1], Elia Bähler[1], Fabian Ospelt[1], Marco Tognon[1], Stefano Mintchev[2], Roland Siegwart[1]

***Abstract*— This work presents the mechanical design and control of a novel small-size and lightweight Micro Aerial Vehicle (MAV) for aerial manipulation. To our knowledge, with a total take-off mass of only 2.0 kg, the proposed system is the most lightweight Aerial Manipulator (AM) that has 8-DOF independently controllable: 5 for the aerial platform and 3 for the articulated arm. We designed the robot to be fully-actuated in the body forward direction. This allows independent pitching and instantaneous force generation, improving the platform's performance during physical interaction. The robotic arm is an origami delta manipulator driven by three servomotors, enabling active motion compensation at the end-effector. Its composite multimaterial links help reduce the weight, while their flexibility allow for compliant aerial interaction with the environment. In particular, the arm's stiffness can be changed according to its configuration. We provide an in depth discussion of the system design and characterize the stiffness of the delta arm. A control architecture to deal with the platform's overactuation while exploiting the delta arm is presented. Its capabilities are experimentally illustrated both in free flight and physical interaction, highlighting advantages and disadvantages of the origami's folding mechanism.**

I. INTRODUCTION

Nowadays, the interest for aerial platforms able to perform manipulation tasks is constantly increasing [1]. Many inspection applications require specifically trained operators working at elevated locations performing interaction and manipulation tasks. On the other hand, the use of AMs would reduce costs and operation time, improving safety as well. The use of multi-directional thrust platforms has been proved fundamental to perform Aerial Physical Interaction (APhI) tasks, being able to independently exert forces and torques. Different configurations of multi-directional thrust systems [2] have already been tested in the past: examples are tricopters [3], quadcopters [4], [5], hexacopters [6] and even octocopters [7].

By enhancing the mobility of a MAV with the dexterity of a robot manipulator, new possibilities are unlocked [8]. Among all possible robotic arms, delta manipulators are of particular interest for aerial manipulation because most of their weight is at the base, reducing the inertia and thus the reaction forces on the aerial platform during the motion. Additionally, they possess very fast dynamics in their three translational degrees of freedom (DOF), allowing them to compensate possible base position offsets or oscillations. This made them a popular choice, both for APhI with quadcopters [9], [10], [11], or end-effector tracking with an omnidirectional platform [12]. However, due to the amount of required actuators, joints and linkages, the addition of actively driven end-effectors often results in a large and heavy system. The work in [13] gives an overview of several AM designs. In particular, it shows that 60% of the reviewed platforms weight more than 2.0 kg. Considering only platforms with manipulators having at least 3 actuated DOF, the lightest setup is based on a standard quadrotor and weights 1.9 kg [9]. Instead, with only 100 g more (total weight of 2.0 kg), we propose a novel overactuated platform, capable of independent pitching, with double the payload.

Apart from the weight, compliance plays an important role in the contact stability during APhI, as already shown in [14], [15]. Despite its importance, the current state-of-the-art platforms still employ rigid-link delta manipulators, sometimes adding small spring elements at the end-effector [9], [11]. This further increases the complexity and weight of the mechanical structure. On the other hand, origami manufacturing allows for the lightweight construction of complex 3D structures through folding composites

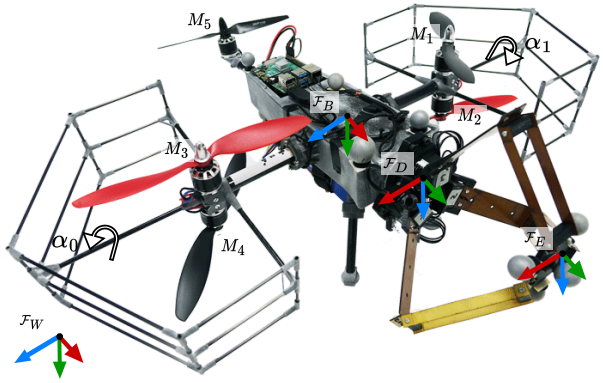

Fig. 1: The overactuated MAV with the origami delta manipulator. The body $\mathcal{F}_B$, world $\mathcal{F}_W$, delta base $\mathcal{F}_D$ and end-effector $\mathcal{F}_E$ frames are shown. The $\boldsymbol{x}$, $\boldsymbol{y}$, $\boldsymbol{z}$ axes are represented in red, blue, green, respectively. The arm tilt angles around the body ${}_B\boldsymbol{y}$ axis are indicated with α_0, α_1.

The research leading to these results has been supported by the AERO-TRAIN project, European Union's Horizon 2020 research and innovation programme under the Marie Skłodowska-Curie grant agreement No 953454, by the Swiss National Science Foundation through the Eccellenza Grant PCEFP2_186865, by NCCR Digital Fabrication, Armasuisse Science and Technology and NCCR Robotics, a National Centre of Competence in Research, funded by the Swiss National Science Foundation (grant number 51NF40_185543). The authors are solely responsible for its content.

[1]Autonomous Systems Laboratory, ETH Zurich, Switzerland.
[2]Environmental Robotics Laboratory, ETH Zurich, Switzerland.
Corresponding author email ecuniato@ethz.ch

of rigid and flexible layers, generating links and joints with inherent flexibility [16]. Specifically for delta robots, origami manufacturing facilitates ease of monolithic construction or miniaturization, such as for haptic user interfaces [17] or centimeter [18] and millimeter scale [19] delta robots.

Despite the compliance and reduced weight of origami manipulators which make them well-suited for aerial applications, their use for aerial manipulation have remained mostly unexplored. In [20], a one DOF unarticulated origami arm was used as an extensible gripper on a MAV, by storing the arm flat during take-off and extending it during flight.

In this work we describe the design and control of a novel small-size, lightweight, and overactuated AM, representing a highly versatile platform for inspection tasks. Its core elements are a tri-tiltrotor MAV with 5 DOFs and an origami delta arm providing additional 3 DOFs (see Fig. 1). The entire system has a take-off mass of $2.0\,\mathrm{kg}$ and its longest side spans a length of only $56\,\mathrm{cm}$. To the best of the authors' knowledge, this represents the lightest 8 DOFs AM in the state-of-the-art. We demonstrate the use of an inherently compliant origami delta manipulator on an aerial robot, which allows for precise motion compensation tasks (as for rigid delta arms), while providing additional compliance during interaction. In particular, we first compute the exact delta kinematics, taking into account the non-idealities of the universal joints approximation. Then, we experimentally characterize the arm compliance and show how this affects the maximum force that the AM can exert on the environment. Moreover we also discuss possible unwanted foldings of the origami joints (which we refer to as *critical configurations*) and provide some insights on how to improve the prototype's robustness.

II. System design

We design the system with the following goals in mind: (i) Small size and light weight platform, to allow operations in confined areas, while increasing safety when operating close to humans. (ii) Power efficiency for long flight times. (iii) Versatility and suitability for inspection tasks, including the ability to accurately touch an arbitrarily oriented surface at a desired location. In order to achieve these goals, we design an overactuated platform augmented with an articulated end-effector. In our case, the overactuation has two main advantages: (i) it allows instantaneous force compensation in the forward interaction direction, and (ii) it allows to hover and perform interaction tasks at different pitching angles. An overview of the AM is illustrated in Fig. 1.

A. Aerial platform

We use the North-East-Down (NED) convention to describe the body frame $\mathcal{F}_B = \{{}_B O, {}_B\boldsymbol{x}, {}_B\boldsymbol{y}, {}_B\boldsymbol{z}\}$, fixed to the Center of Mass (CoM) of the MAV, as well as the inertial world frame $\mathcal{F}_W = \{{}_W O, {}_W\boldsymbol{x}, {}_W\boldsymbol{y}, {}_W\boldsymbol{z}\}$, as illustrated in Fig. 1. The chosen multirotor configuration consists of two groups of coaxial rotors, which can tilt around the ${}_B\boldsymbol{y}$ axis, and a rear motor with a bidirectional propeller. The propellers and tilt arms have complete control authority over the generated body torques, as well as forces along the ${}_B\boldsymbol{z}$ and ${}_B\boldsymbol{x}$ axes. Since forces along ${}_B\boldsymbol{y}$ cannot be generated with the chosen configuration (they are always zero), the linear and angular dynamics in this direction are coupled.

Part	MAV (g)	Delta (g)
Battery	540	-
Motors	375	135
Structure	345	130
Electronics	230	25
Others	150	10
Bumpers	60	-
Total	1700	300

TABLE I: Weight (in grams) of the AM components.

Component	Name	Qty.
Motor	KDE2315XF-885	5
ESC	Tekko32 F3	5
Origami servo	Dynamixel XL-330	3
Tiltrotor servo	Dynamixel XL-320	2
Buck Converter	Henge 8A UBEC	2
Flight controller	Pixhawk Cube Grey	1
Battery	Zop 4S 5000mAh	1
PDB	Pixhawk 4 Mini PDB	1
RC Receiver	Jeti PPM Receiver	1
Onboard computer	Raspberry Pi 4B	1

TABLE II: Electrical components of the AM.

The MAV is intentionally built to fit inside small manholes and to operate in closed environments. Without propeller guards it measures $55\,\mathrm{cm}$ in length and $56\,\mathrm{cm}$ in width. The propellers of the two main rotor groups are 9"x4.7 while the rear 3D propeller measures 8"x4.5. It weights $1.7\,\mathrm{kg}$ and can transport a maximum additional payload of $1\,\mathrm{kg}$. The main frame and all the other structural parts are printed with Nylon PA12 using a HP Multi Jet Fusion 3D printer, apart from motor arms and tail that are made of carbon tubes. The biggest contribution on the weight comes from a $5000\,\mathrm{mAh}$ 4S battery ($540\,\mathrm{g}$), which experimentally reflected in around 18 minutes of flight time without additional payload. Another experimental test with $0.8\,\mathrm{kg}$ of payload, for a total weight of $2.5\,\mathrm{kg}$, resulted in 7 minutes of flight time. A summary of the weight contributions of the different components is in table I. A voltage buck converter provides $5\,\mathrm{V}$ to power the Pixhawk flight controller, onboard computer and delta arm, while another provides $7.5\,\mathrm{V}$ for the two Dynamixels XL-320 moving the arms. Table II gives an overview of the platform's electrical components.

B. Origami-based delta manipulator

The design of the origami manipulator is shown in Fig. 2. Delta parallel arms consist of three identical legs connecting the moving end-effector plate to the fixed base platform. Each of the legs is driven by a one DOF rotary servomotor connected to the base platform. The legs consist of proximal and distal limbs, the latter formed by parallel bars, creating a quadrilateral parallelogram-like structure. This results in pure translation motions between base and end-effector [21].

In ideal delta manipulators, the joints between the proximal limbs, the parallelogram linkages and the end-effector plate are universal joints. For the origami manipulator, the

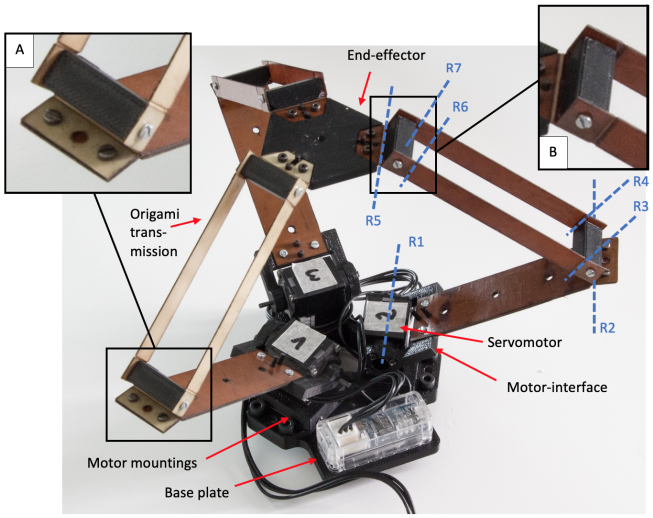

Fig. 2: Design of the origami-based delta manipulator with the main components highlighted. The details (A) and (B) show the approximation of the universal joints using perpendicular revolute joints. The dashed lines indicate the rotation axes of each joint.

universal joints are approximated using the solution proposed in [17], [19]. The side linkages of the parallelogram are folded upwards and an additional fold is added close to both ends of the linkages (Fig. 2(A)). This results in perpendicular revolute joints at the knee (R2, R3 and R4) and ankle (R5, R6 and R7) of the parallelogram, approximating the universal joints. Unlike conventional delta robots, here the rotation axes do not coincide, resulting in a different kinematic model. Even if new origami designs were proposed in order to remove the universal joint approximation [18], we prefer to avoid having one monolitic arm structure. The origami limbs are attached to the 3D printed motor-interface and end-effector plate with screws and alignment pins, which allow easy replacement in case of breaking of an arm's element [22]. Moreover we will derive the exact arm kinematics even in the presence of non-universal joints.

The origami structures are made of a three layer, multi-material composite. The top and bottom layers are made of fiberglass (FR-4-HF, 0.3mm), which provides the necessary stiffness. The middle Kapton layer with adhesive on both sides (DuPont Pyralux LF0111, 0.05mm) adds the necessary flexibility at the joints and bonds layers together. Each layer is individually laser-cut with a CO_2 laser (Trotec Speedy 360), stacked, and then aligned by pins and holes. The layers are then bonded together by the adhesive on the surfaces of the Kapton layer using a hydraulic heat press (Fontjine LabManual 300). The upper and lower limbs are built separately and then screwed together at the knee joints, reducing material waste and simplifying the pattern. The other structural parts were printed with ABS.

The use of foldable joints instead of mechanical joints gives a compliant behavior to the delta robot. This inherent flexibility depends not only on the design parameters (e.g., joint geometry and material properties), but also on the configuration assumed by the manipulator. This allows adjusting the compliance of the manipulator to the requirements of the task. For example, a soft configuration is conducive to safer interactions, while a stiffer configuration may be preferred to achieve greater accuracy and repeatability. In Sec. IV we characterize the axial stiffness of the manipulator and show how it influences a simple interaction task.

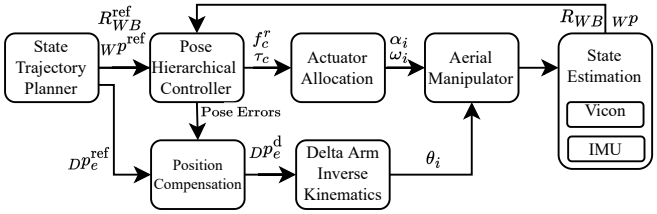

Fig. 3: Control scheme of the Aerial Manipulator.

III. Control Design

In this section we present the control design of the AM, which is schematically presented in Fig. 3. First, we develop a pose control law for the overactuated MAV modifying the geometric controller for quadrotors in [23]. Secondly, we derive the Inverse Kinematics (IK) for the origami delta arm, coupling it to the MAV's pose.

A. Aerial platform pose control

Consider the inertial world frame $\mathcal{F}_W$ and the body frame $\mathcal{F}_B$ attached to the MAV in its CoM. We define ${}_W\boldsymbol{p}$ as the position of the body frame's origin in $\mathcal{F}_W$ and $\boldsymbol{R}_{BW} \in \mathrm{SO}(3)$ as the rotation matrix from $\mathcal{F}_W$ to $\mathcal{F}_B$. The position and attitude dynamics of the MAV are then given by

$$m\left({}_B\dot{\boldsymbol{v}} + {}_B\boldsymbol{\omega} \times {}_B\boldsymbol{v}\right) = {}_B\boldsymbol{f}_g + {}_B\boldsymbol{f}_c \tag{1a}$$

$$\boldsymbol{J}\,{}_B\dot{\boldsymbol{\omega}} + {}_B\boldsymbol{\omega} \times \boldsymbol{J}\,{}_B\boldsymbol{\omega} = \boldsymbol{\tau}_c, \tag{1b}$$

where $m \in \mathbb{R}$ is the total mass of the platform, $\boldsymbol{J} \in \mathbb{R}^{3\times3}$ is the inertia matrix in $\mathcal{F}_B$, $\boldsymbol{f}_g \in \mathbb{R}^3$ is the gravity force vector, $\boldsymbol{v}, \boldsymbol{\omega} \in \mathbb{R}^3$ are the platform's linear and angular velocity, and $\boldsymbol{f}_c, \boldsymbol{\tau}_c \in \mathbb{R}^3$ are the force and torque commands, respectively. Since the system cannot produce instantaneous thrust along its body ${}_B\boldsymbol{y}$ axis, we employ a cascaded control structure with an outer loop position controller and an inner loop attitude controller. Consider the position and velocity errors of the linear dynamics as

$${}_B\boldsymbol{e}_p = \boldsymbol{R}_{BW}\left({}_W\boldsymbol{p}^{\text{ref}} - {}_W\boldsymbol{p}\right) \tag{2a}$$

$${}_B\boldsymbol{e}_v = \boldsymbol{R}_{BW}\,{}_W\boldsymbol{v}^{\text{ref}} - {}_B\boldsymbol{v}, \tag{2b}$$

where $\boldsymbol{e}_p, \boldsymbol{e}_v \in \mathbb{R}^3$ are the position and velocity errors, respectively, and the quantities $(\cdot)^{\text{ref}}$ are generated by a suitable trajectory planner. Based on (2) we define the Proportional-Derivative (PD) control law as

$$\begin{aligned}{}_B\boldsymbol{f}_c = \boldsymbol{K}_p\,{}_B\boldsymbol{e}_p + \boldsymbol{D}_p\,{}_B\boldsymbol{e}_v - {}_B\boldsymbol{f}_g + \\ + m\left(\boldsymbol{R}_{BW}\,{}_W\dot{\boldsymbol{v}}^{\text{ref}} + {}_B\boldsymbol{\omega} \times {}_B\boldsymbol{v}\right).\end{aligned} \tag{3}$$

For the attitude control loop, consider the reference orientation given by $\boldsymbol{R}^{\text{ref}}_{WB} = \left[{}_B\boldsymbol{x}^{\text{ref}} \;\; {}_B\boldsymbol{y}^{\text{ref}} \;\; {}_B\boldsymbol{z}^{\text{ref}}\right] \in \mathrm{SO}(3)$ that

contains the pitch and yaw angle references of $\mathcal{F}_B$ w.r.t. $\mathcal{F}_W$ (note that, given the platform's actuation, only yaw and pitch can be tracked individually).

We then construct the attitude-loop target orientation, denoted by $\boldsymbol{R}^d_{WB} \in \mathrm{SO}(3)$, as follows. We first define a new command vector ${}_B\bar{\boldsymbol{f}}_c = [0 \;\; {}_Bf_{c,y} \;\; {}_Bf_{c,z}]^\top$, from which the commanded force along ${}_Bx$ has been removed. We then rotate it into $\mathcal{F}_W$ and compute the desired body-frame z-axis, expressed in the world frame, as ${}_B\boldsymbol{z}^d := \frac{{}_W\bar{\boldsymbol{f}}_c}{\|{}_W\bar{\boldsymbol{f}}_c\|}$. Lastly, we compute ${}_B\boldsymbol{y}^d = \frac{{}_B\boldsymbol{z}^d \times {}_B\boldsymbol{x}^{\text{ref}}}{\|{}_B\boldsymbol{z}^d \times {}_B\boldsymbol{x}^{\text{ref}}\|}$ and obtain the desired rotation matrix for the inner attitude control loop as

$$\boldsymbol{R}^d_{WB} = \begin{bmatrix} {}_B\boldsymbol{x}^{\text{ref}} & {}_B\boldsymbol{y}^d & \frac{{}_B\boldsymbol{x}^{\text{ref}} \times {}_B\boldsymbol{y}^d}{\|{}_B\boldsymbol{x}^{\text{ref}} \times {}_B\boldsymbol{y}^d\|} \end{bmatrix}. \tag{4}$$

Note how the desired rotation matrix in (4) preserves the reference pitch and yaw angles, while exploiting the roll dynamics to pursue the position tracking task. We now define the inner attitude loop control errors as

$${}_B\boldsymbol{e}_R = \frac{1}{2}\left[\boldsymbol{R}^d_{WB}{}^\top \boldsymbol{R}_{WB} - \boldsymbol{R}^\top_{WB}\boldsymbol{R}^d_{WB}\right]^\vee, \tag{5a}$$

$${}_B\boldsymbol{e}_\omega = {}_B\boldsymbol{\omega} - \boldsymbol{R}_{WB}\,{}_W\boldsymbol{\omega}^{\text{ref}}, \tag{5b}$$

where $(\cdot)^\vee : \mathfrak{so}(3) \to \mathbb{R}^3$ is the vee operator which transforms a skew-symmetric matrix to a vector. Then, the control torque command ${}_B\boldsymbol{\tau}_c \in \mathbb{R}^3$ can be computed as

$$\begin{aligned} {}_B\boldsymbol{\tau}_c = {} & \boldsymbol{K}_R\boldsymbol{e}_R + \boldsymbol{D}_\omega\boldsymbol{e}_\omega + \boldsymbol{\omega}\times\boldsymbol{J}\boldsymbol{\omega} + \\ & - \boldsymbol{J}\left[\boldsymbol{\omega}\times\boldsymbol{R}^\top_{WB}\boldsymbol{R}^d_{WB}\boldsymbol{\omega}^{\text{ref}} - \boldsymbol{R}^\top_{WB}\boldsymbol{R}^d_{WB}\dot{\boldsymbol{\omega}}^{\text{ref}}\right] \end{aligned} \tag{6}$$

where $\boldsymbol{K}_R,\ \boldsymbol{D}_\omega \in \mathbb{R}^{3\times3}$ are diagonal and positive gain matrices. All quantities are expressed in $\mathcal{F}_B$ and the ${}_B(\cdot)$ subscript has been omitted for brevity.

Actuator allocation: In order to compute the actuator commands from the force and torque control commands, we compute the *actuator allocation* as follows. We define T_{12} and T_{34} as the thrusts produced by the respective motor groups, and α_0 and α_1 as the tilt angles of the two arms, as showed in Fig. 1. Furthermore, l_1 is the distance from the center of the two frontal motor groups to the origin of $\mathcal{F}_B$, and l_2 the distance from the center of the tail motor to the to the origin of $\mathcal{F}_B$. Considering the MAV geometry, the actuator allocation is given by the equations

$$\begin{bmatrix} \boldsymbol{f}^r_c \\ \boldsymbol{\tau}_c \end{bmatrix} = \underbrace{\begin{bmatrix} 1 & 0 & -1 & 0 & 0 \\ 0 & -1 & 0 & -1 & -1 \\ 0 & l_1 & 0 & -l_1 & 0 \\ 0 & 0 & 0 & 0 & -l_2 \\ l_1 & 0 & l_1 & 0 & -k_d \end{bmatrix}}_{\boldsymbol{A}} \underbrace{\begin{bmatrix} T_{12}\sin(\alpha_1) \\ T_{12}\cos(\alpha_1) \\ T_{34}\sin(\alpha_0) \\ T_{34}\cos(\alpha_0) \\ T_5 \end{bmatrix}}_{\boldsymbol{u}}, \tag{7}$$

with $\boldsymbol{f}^r_c = [{}_Bf_{c,x} \;\; {}_Bf_{c,z}]^\top$ containing only command forces along ${}_B\boldsymbol{x}$ and ${}_B\boldsymbol{z}$. Given a set of control forces and torques (i.e. *wrench*), we compute the input vector $\boldsymbol{u}$ as

$$\boldsymbol{u} = \boldsymbol{A}^{-1}\begin{bmatrix} \boldsymbol{f}^r_c \\ \boldsymbol{\tau}_c \end{bmatrix}, \tag{8}$$

and solve for the individual actuator commands:

$$\begin{aligned} T_{12} = \sqrt{u_0^2 + u_1^2}; \quad T_{34} = \sqrt{u_2^2 + u_3^2}; \quad T_5 = u_5 \\ \alpha_0 = \operatorname{atan2}(u_1, u_2); \quad \alpha_1 = \operatorname{atan2}(u_3, u_4). \end{aligned} \tag{9}$$

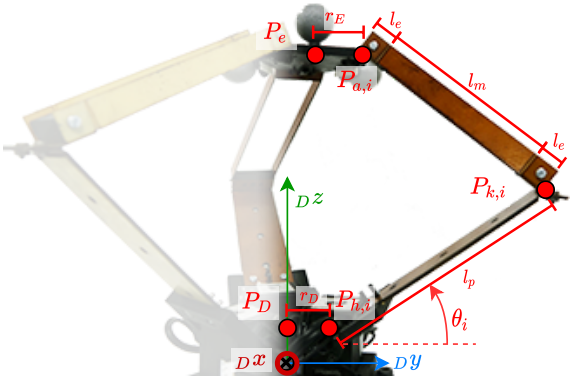

Fig. 4: Schematics of the origami arm.

From there the rotational speeds of the motors can be calculated by using the motor coefficients $k_f,\ k_{f,\text{rear}} \in \mathbb{R}$ and assuming a quadratic relationship

$$\begin{aligned} \omega_1 = \omega_2 = \sqrt{\frac{T_{12}}{2k_f}}; \quad \omega_3 = \omega_4 = \sqrt{\frac{T_{34}}{2k_f}} \\ \omega_5 = \operatorname{sign}(T_5)\sqrt{\frac{\|T_5\|}{k_{f,\text{rear}}}}. \end{aligned} \tag{10}$$

Note that the sign of the rear thrust T_5 must be specifically taken into account, since the rear motor is bidirectional.

Also, with $k_f = 8.1\times10^{-6}\,\mathrm{N\,s^2}$, $k_{f,\text{rear}} = 4.05\times10^{-6}\,\mathrm{N\,s^2}$ and maximum rotor speed $\omega_{\max} = 1143\,\mathrm{rad}$, the platform achieves a maximum total thrust of $T_{\max} = 4.85\,\mathrm{kg}$, which corresponds to a thrust-to-weight ratio of 2.43, considering the full AM. This relatively high ratio allowed never entering into actuator saturation in the proposed experiments.

B. Origami-based delta manipulator inverse kinematics

In this section we describe an IK approach to find the manipulator joint angles θ_i as function of the end-effector target position ${}_D\boldsymbol{p}^d_e$. We express the position of the end-effector frame $\mathcal{F}_E = \{{}_EO, {}_E\boldsymbol{x}, {}_E\boldsymbol{y}, {}_E\boldsymbol{z}\}$ in the delta frame $\mathcal{F}_D = \{{}_DO, {}_D\boldsymbol{x}, {}_D\boldsymbol{y}, {}_D\boldsymbol{z}\}$, which is fixed to the base plate of the arm, as in Fig. 4. We exploit the solution for conventional delta robots [24] with some adjustments to account for the kinematic differences of the origami adaptation.

Consider the geometric description of the origami delta arm in Fig. 4. The solution for a conventional delta robot is given by finding the intersection point $P_{k,i}$ of a circle around the hip joint $P_{h,i}$ with radius l_p and a sphere around the ankle joint $P_{a,i}$ with radius $l_d = l_m + 2l_e$. However, since in the origami design the universal joints do not have aligned rotation axes, the length of the distal link l_d does not remain constant. Therefore, we replace l_d with an expression $l_{d,i}({}_D\boldsymbol{p}_e)$, which depends on the dimensions l_m and l_e as before, but is a function of the end-effector position as well.

The kinematic relation for a generic leg $i = \{1, 2, 3\}$ is

$$\|\boldsymbol{l}_{d,i}\|^2 = \|{}_D\boldsymbol{p}_e + {}_D\boldsymbol{p}_{ai} - {}_D\boldsymbol{p}_{hi} - {}_D\boldsymbol{l}_{ki-hi}(\theta_i)\|^2, \tag{11}$$

with ${}_D\boldsymbol{l}_{ki-hi} = [0 \;\; l_p\cos\theta_i \;\; l_p\sin\theta_i]^\top$ depending on the joint angle. From geometric considerations on the distal link

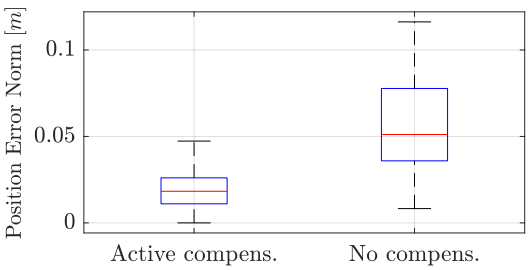

Fig. 5: Position error norm at the end-effector with and without active compensation. The two distributions are positively skewed with medians $0.02\,\mathrm{m}$ and $0.05\,\mathrm{m}$, respectively.

parallelogram, we compute its true length as

$$l_{d,i}({}_D\boldsymbol{p}_e) = \sqrt{p_{e,\parallel}^2 + \left(\sqrt{l_m^2 - p_{e,\parallel}^2} + 2l_e\right)^2}, \tag{12}$$

with $p_{e,\parallel}$ the component of ${}_D\boldsymbol{p}_e$ parallel to the P_{hi} joint axis. Then, by combining (11) and (12), we get

$$0 = E_i \cos\theta_i + F_i \sin\theta_i + G_i, \tag{13a}$$
$$E_i = 2l_p(r_{DE} - {}_Dp_{E,y}), \tag{13b}$$
$$F_i = -2\,{}_Dp_{E,z} l_p, \tag{13c}$$
$$G_i = {}_Dp_{E,x}^2 + {}_Dp_{E,y}^2 + {}_Dp_{E,z}^2 + r_{DE}^2 + l_p^2 - 2\,{}_Dp_{E,y} r_{DE} - l_{d,i}^2, \tag{13d}$$

with $r_{DE} = r_D - r_E$. Finally, in order to compute the desired joint angles θ_i for the end-effector to reach a target position ${}_D\boldsymbol{p}_e^d$, we set ${}_D\boldsymbol{p}_e = {}_D\boldsymbol{p}_e^d$ and solve (13) as[1]

$$\theta_i({}_D\boldsymbol{p}_e^d) = 2\tan^{-1}\left(\frac{-F_i + \sqrt{E_i^2 + F_i^2 - G_i^2}}{G_i - E_i}\right). \tag{14}$$

The desired joint angles are then tracked by the servomotors' integrated PID controllers.

C. Kinematic coupling law

To control both the MAV body and the delta arm, we couple the two frames $\mathcal{F}_B$ and $\mathcal{F}_E$ kinematically. This aims to compensate any oscillations occurring in the body pose tracking error ${}_B\boldsymbol{e}_p$. To this end, we adapt the end-effector position reference ${}_D\boldsymbol{p}_e^{\text{ref}}$ according to ${}_B\boldsymbol{e}_p$, generating the instantaneous end-effector target ${}_D\boldsymbol{p}_e^d$.

$${}_D\boldsymbol{p}_e^d = {}_D\boldsymbol{p}_e^{\text{ref}} + \boldsymbol{R}_{DB}\,{}_B\boldsymbol{e}_p + \boldsymbol{R}_{DB}\boldsymbol{R}_{WB}^{\text{ref}\,\top}\boldsymbol{R}_{WB}\,{}_B\boldsymbol{p}_{BD}, \tag{15}$$

where ${}_B\boldsymbol{p}_{BD} \in \mathbb{R}^3$ is the distance between the origins of the $\mathcal{F}_D$ and $\mathcal{F}_B$ expressed in $\mathcal{F}_B$ and $\boldsymbol{R}_{WB}^{\text{ref}\,\top}\boldsymbol{R}_{WB}$ accounts for rotational errors. The instantaneous target ${}_D\boldsymbol{p}_e^d$ is then used to compute the desired joint angles θ_i.

IV. Experimental Results

In this section, we focus specifically on three aspects: (i) The end-effector position tracking performance during free flight, (ii) a characterization of the origami manipulator stiffness depending on its configuration, and (iii) the system characteristics during interaction, particularly the achievable interaction forces with different manipulator stiffness.

[1]We employed the tangent half-angle substitution to solve this equation.

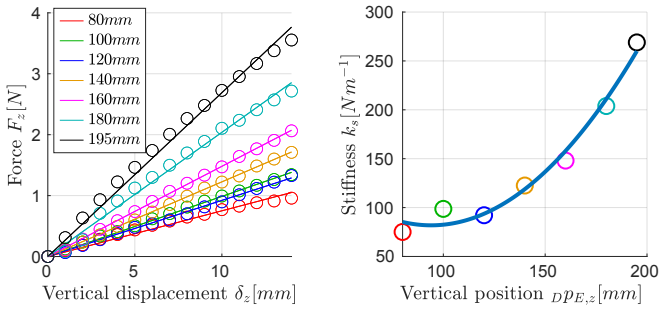

(a) Linear spring model fits at different heights ${}_Dp_{E,z}$.

(b) Stiffness interpolation over height.

Fig. 6: Origami delta arm stiffness identification.

A. Manipulator kinematic compensation

In this experiment, we evaluate the positioning accuracy of the AM's end-effector. To perform this analysis, we command a constant end-effector reference pose and we track it only using the MAV, with the origami arm in a fixed configuration. After recording a sufficient number of samples, the delta arm is actively commanded to compensate for the floating base displacements. The end-effector position is obtained from the arm's forward kinematics. The performances in the two scenarios are in Fig. 5. The median and interquartile range of the tracking error's norm is more than halved in active compensation with respect to the fixed arm case.

B. Origami manipulator stiffness characterization

Here we model the manipulator's stiffness in different positions of the end-effector frame $\mathcal{F}_E$ with respect to the delta base frame $\mathcal{F}_D$. Specifically, the origin of $\mathcal{F}_E$ was always kept along the vertical direction ${}_D\boldsymbol{z}$. These measurements were taken by attaching the manipulator on a load cell and pressing down the end-effector plate in one millimeter increments along the ${}_D\boldsymbol{z}$ direction. Both end-effector position displacements $\delta_z \in \mathbb{R}$ and push force $F_z \in \mathbb{R}$ were recorded for each chosen end-effector height value ${}_Dp_{E,z}$. In the end, a linear spring model was fitted for different height values as $F_z = k_s\delta_z$, with $k_s({}_Dp_{E,z})$ the estimated end-effector stiffness. The different stiffness fittings are visible in Fig. 6a. In particular, different data points have been collected at heights in the range ${}_Dp_{E,z} \in [80,\ 195]\,\mathrm{mm}$, interpolating the resulting stiffness with a second order polynomial $k_s({}_Dp_{E,z}) = c_0 + c_1\,{}_Dp_{E,z} + c_2\,{}_Dp_{E,z}^2$, where c_0,c_1,$c_2 \in \mathbb{R}$ are the identified coefficients. We choose a second-order curve to balance complexity and fitting error. The resulting interpolation is shown in Fig. 6b, with a stiffness change in the range $k_s \in [80\ 290]\,\mathrm{N\,m^{-1}}$. Note that the stiffness is greater when the arm is fully extended, whereas it is most compliant with the arm retracted. Having a mechanically variable stiffness arm represents an advantage when it is not possible to implement a software impedance control action. For instance, this is the case when the mathematical model of the MAV is not known with enough precision for an impedance controller, or when only position control is available without an external force and torque (F/T) sensor or

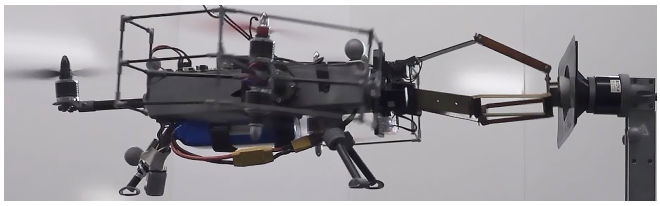

Fig. 7: APhI experiment with the AM pushing on a surface connected to a F/T sensor.

estimator to implement an admittance control scheme. Note that the stiffness characterization is performed considering a centered end-effector since we assume to only interact with the environment in this condition. A complete characterization, although possible, would require much more experimental data and is beyond the scope of this work. Here we aim at providing preliminary results on how the compliance influences the interaction contact forces, whereas a full exploitation will be addressed in future works.

C. Physical interaction

To study the different behaviors and exerted forces depending on the commanded stiffness configuration of the manipulator, a physical interaction experiment was conducted as shown in Fig. 7. We commanded the AM to approach a surface and push against it with the origami manipulator configured at different stiffness levels. The surface was connected to a F/T sensor to provide ground truth data of the pushing forces. Once in contact, the origami arm's stiffness k_s was increased up to $290\,\mathrm{N\,m^{-1}}$. This resulted in a subsequent increase of the pushing force, as in Fig. 8a. The origami manipulator was able to sustain a peak force of $4\,\mathrm{N}$ before the structure folded into a critical configuration. Similarly, another experiment was conducted with the lowest stiffness allowed by the manipulator, while pushing further with the aerial base, in Fig. 8b. Here, the AM was exerting a force of $2\,\mathrm{N}$ when the critical folding occurred.

The *critical folding configurations* are phenomenons due to an unnatural bending of the origami joints, from which the AM can't autonomously recover, as in Fig. 9. We refer to *knee* or *ankle critical folding* as the ones caused by the bending of one of the knee or ankle joints, respectively. The former is likely to happen when pushing too strongly on the fully extended origami arm, i.e., in a high-stiffness configuration. The latter happens when pushing too much on the retracted origami arm, in a low-stiffness configuration. Manipulator configurations at the center of the stiffness spectrum were generally less prone to fold into critical configurations. Identifying these particular configurations is of primary importance to describe the arm's feasible workspace and exerted forces, to avoid criticalities in more complex tasks, where reliability plays a fundamental role. In particular, future designs of the origami manipulator will feature mechanic stoppers at joints $R5$ to prevent the *ankle critical folding*, while increasing the robustness of joints $R3$ and $R4$ will prevent the *knee critical folding*.

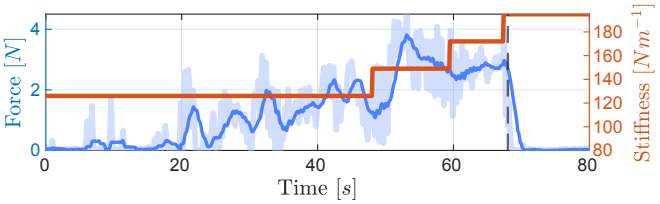

(a) Interaction with increasing stiffness.

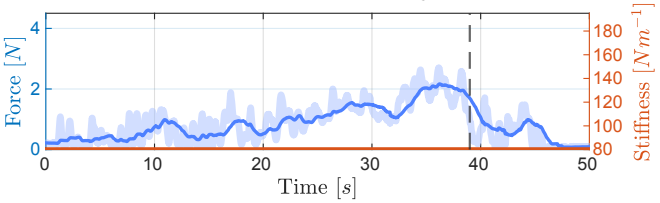

(b) Interaction with constant low stiffness.

Fig. 8: Interaction force (blue) generated with different stiffness configurations (red). The dashed vertical line represents the time instant of the origami critical folding. The transparent blu shadow represents the unfiltered force measurements. The solid blue line is a filtered version for the graph's clarity.

Fig. 9: Knee (left) and ankle (right) critical foldings.

V. CONCLUSIONS

We realized a small and lightweight AM for inspection purposes. We first described the construction process of both the aerial platform and the origami arm and how a very low weight can be reached with a careful choice of design and building materials. We then derived a pose controller for the body and an IK controller for the manipulator, coupling them to achieve accurate pose tracking of the end-effector. We showed how the addition of the origami manipulator increases the end-effector tracking performance in free-flight and how the manipulator compliance can be adjusted during APhI, affecting the generated interaction forces. We validated the use of inherently compliant manipulators as opposed to the rigid counterparts with additional spring elements, which would increase the system's weight and complexity. In the end, we also analyzed its limitations when it comes to undesirable arm foldings. We believe that in future work, adjusting the manipulator compliance in such a high range will be a key element in more complex interaction scenarios, increasing both the robustness and safety of APhI tasks. We will also further address the problem of the critical folding configurations, leading to a more robust mechanical design.

ACKNOWLEDGMENT

We thank Christoph Gaupp for his help on building the MAV platform prototype.

REFERENCES

[1] A. Ollero, M. Tognon, A. Suarez, D. Lee, and A. Franchi, "Past, present, and future of aerial robotic manipulators," *IEEE Transactions on Robotics*, vol. 38, no. 1, pp. 626–645, 2022.

[2] M. Hamandi, F. Usai, Q. Sablé, N. Staub, M. Tognon, and A. Franchi, "Design of multirotor aerial vehicles: A taxonomy based on input allocation," *The International Journal of Robotics Research*, vol. 40, no. 8-9, pp. 1015–1044, 2021.

[3] C. Papachristos, K. Alexis, and A. Tzes, "Efficient force exertion for aerial robotic manipulation: Exploiting the thrust-vectoring authority of a tri-tiltrotor uav," in *2014 IEEE International Conference on Robotics and Automation (ICRA)*, 2014, pp. 4500–4505.

[4] M. Ryll, H. H. Bülthoff, and P. R. Giordano, "Modeling and control of a quadrotor uav with tilting propellers," in *2012 IEEE International Conference on Robotics and Automation*, 2012, pp. 4606–4613.

[5] A. B. Junaid, A. D. D. C. Sanchez, J. B. Bosch, N. I. Vitzilaios, and Y. H. Zweiri, "Design and implementation of a dual-axis tilting quadcopter," *Robotics*, vol. 7, p. 65, 2018.

[6] M. S. Kamel, S. Verling, O. Elkhatib, C. Sprecher, P. Wulkop, Z. Taylor, R. Siegwart, and I. Gilitschenski, "The voliro omnidirectional hexacopter: An agile and maneuverable tiltable-rotor aerial vehicle," *IEEE Robotics & Automation Magazine*, vol. PP, pp. 1–1, 10 2018.

[7] D. Brescianini and R. D'Andrea, "Design, modeling and control of an omni-directional aerial vehicle," in *IEEE International Conference on Robotics and Automation (ICRA)*, 2016, pp. 3261–3266.

[8] M. Tognon, H. A. Tello-Chavez, E. Gasparin, Q. Sablé, D. Bicego, A. Mallet, M. Lany, G. Santi, B. Revaz, J. Cortés, and A. Franchi, "A truly-redundant aerial manipulator system with application to push-and-slide inspection in industrial plants," *IEEE Robotics and Automation Letters*, vol. 4, pp. 1846–1851, 01/2019 2019.

[9] M. Fumagalli, R. Naldi, A. Macchelli, F. Forte, A. Q. Keemink, S. Stramigioli, R. Carloni, and L. Marconi, "Developing an Aerial Manipulator Prototype: Physical Interaction with the Environment," *IEEE Robotics & Automation Magazine*, vol. 21, pp. 41–50, 2014.

[10] P. Chermprayong, K. Zhang, F. Xiao, and M. Kovac, "An integrated delta manipulator for aerial repair: A new aerial robotic system," *IEEE Robotics & Automation Magazine*, vol. 26, no. 1, pp. 54–66, 2019.

[11] D. Tzoumanikas, F. Graule, Q. Yan, S. Dhruv, M. Popovic, and S. Leutenegger, "Aerial manipulation using hybrid force and position nmpc applied to aerial writing," in *Robotics: Science and Systems (RSS)*, 2020.

[12] K. Bodie, M. Tognon, and R. Siegwart, "Dynamic End Effector Tracking With an Omnidirectional Parallel Aerial Manipulator," *IEEE Robotics and Automation Letters*, vol. 6, no. 4, pp. 8165–8172, 2021.

[13] X. Meng, Y. He, and J. Han, "Survey on aerial manipulator: System, modeling, and control," *Robotica*, vol. 38, pp. 1288 – 1317, 2019.

[14] A. Suarez, G. Heredia, and A. Ollero, "Lightweight compliant arm with compliant finger for aerial manipulation and inspection," in *2016 IEEE/RSJ International Conference on Intelligent Robots and Systems (IROS)*. IEEE, 2016, pp. 4449–4454.

[15] T. Bartelds, A. Capra, S. Hamaza, S. Stramigioli, and M. Fumagalli, "Compliant aerial manipulators: Toward a new generation of aerial robotic workers," *IEEE Robotics and Automation Letters*, vol. 1, no. 1, pp. 477–483, 2016.

[16] D. Rus and M. T. Tolley, "Design, fabrication and control of origami robots," *Nature Reviews Materials*, vol. 3, no. 6, pp. 101–112, 2018.

[17] S. Mintchev, M. Salerno, A. Cherpillod, S. Scaduto, and J. Paik, "A portable three-degrees-of-freedom force feedback origami robot for human–robot interactions," *Nature Machine Intelligence*, vol. 1, no. 12, pp. 584–593, dec 2019.

[18] M. A. Kalafat, H. Sevinç, S. Samankan, A. Altınkaynak, and Z. Temel, "A Novel Origami-Inspired Delta Mechanism With Flat Parallelogram Joints," *Journal of Mechanisms and Robotics*, vol. 13, no. 2, apr 2021.

[19] H. McClintock, F. Z. Temel, N. Doshi, J.-s. Koh, and R. J. Wood, "The milliDelta: A high-bandwidth, high-precision, millimeter-scale Delta robot," *Science Robotics*, vol. 3, no. 14, jan 2018.

[20] S.-J. Kim, D.-Y. Lee, G.-P. Jung, and K.-J. Cho, "An origami-inspired, self-locking robotic arm that can be folded flat," *Science Robotics*, vol. 3, no. 16, p. eaar2915, mar 2018.

[21] L. Rey and R. Clavel, "The delta parallel robot," in *Parallel Kinematic Machines*, C. R. Boër, L. Molinari-Tosatti, and K. S. Smith, Eds. London: Springer London, 1999, pp. 401–417.

[22] M. Salerno, J. Paik, and S. Mintchev, "Ori-pixel, a multi-dofs origami pixel for modular reconfigurable surfaces," *IEEE Robotics and Automation Letters*, vol. 5, no. 4, pp. 6988–6995, 2020.

[23] T. Lee, M. Leok, and N. H. McClamroch, "Geometric tracking control of a quadrotor uav on se(3)," in *49th IEEE Conference on Decision and Control (CDC)*, 2010, pp. 5420–5425.

[24] R. L. Williams II, "The delta parallel robot: Kinematics solutions," January 2016, internet Publication.